HHS Public Access

Author manuscript

Cell Chem Biol. Author manuscript; available in PMC 2017 December 22.

Published in final edited form as:

Cell Chem Biol. 2016 December 22; 23(12): 1449–1457. doi:10.1016/j.chembiol.2016.10.013.

Fluorescent Visualization of Cellular Proton Fluxes

Lejie Zhang[1,2], **Karl Bellve**[3], **Kevin Fogarty**[3], and **William R. Kobertz**[1,2,*]

[1]Department of Biochemistry and Molecular Pharmacology, University of Massachusetts Medical School, 364 Plantation Street, Worcester, MA 01605-2324

[2]Programs in Neuroscience and Chemical Biology, University of Massachusetts Medical School, 364 Plantation Street, Worcester, MA 01605-2324

[3]Biomedical Imaging Group, Molecular Medicine, University of Massachusetts Medical School, 364 Plantation Street, Worcester, MA 01605-2324

Summary

Cells use plasma membrane proton fluxes to maintain cytoplasmic and extracellular pH and to mediate the co-transport of metabolites and ions. Because proton-coupled transport often involves movement of multiple substrates, traditional electrical measurements provide limited information about proton transport at the cell surface. Here we visualize voltage-dependent proton fluxes over the entire landscape of a cell by covalently attaching small molecule fluorescent pH sensors to the cell's glycocalyx. We found that the extracellularly-facing sensors enable real-time detection of proton accumulation and depletion at the plasma membrane, providing an indirect readout of channel and transporter activity that correlated with whole-cell proton current. Moreover, the proton wavefront emanating from one cell was readily visible as it crossed over nearby cells. Given that any small molecule fluorescent sensor can be covalently attached to a cell's glycocalyx, our approach is readily adaptable to visualize most electrogenic and non-electrogenic transport events at the plasma membrane.

Graphical abstract

[*]Address correspondence to the "Lead Contact": Dr. William R. Kobertz, Department of Biochemistry and Molecular Pharmacology, University of Massachusetts Medical School, 364 Plantation Street, Worcester, MA 01605-2324, 508.856.8861 (phone), 508.856.8867 (fax), william.kobertz@umassmed.edu.

The authors declare that they have no competing financial interests.

Author contributions: LZ and WRK designed the experiments and wrote the manuscript. Patch clamp fluorometry setup was built by KB; initial experiments were performed on "Scratch" and TIRF images were acquired on TESM, which were built and maintained by KF and KB. LZ performed all of the experiments and data analysis. All authors have approved the final version of the manuscript.

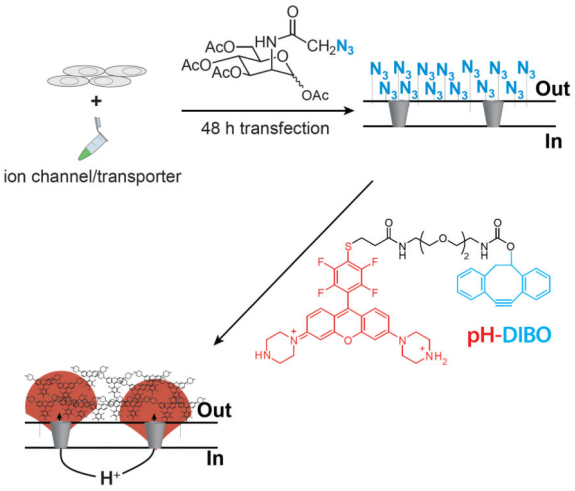

Keywords

voltage-gated; ion channels; membrane transport; pH; glycocalyx

Introduction

Proton fluxes at the plasma membrane are mediated by voltage-gated proton channels (Hv-1) and proton-coupled membrane transporters that concomitantly transport a proton with another substrate in the same (co-transporter) or opposite (antiporter) direction. Rapid proton transport through these membrane-embedded proteins is essential for maintaining intracellular pH (Decoursey, 2003), regulating gastric (Kopic and Geibel, 2013) and airway mucosal acidity (Fischer and Widdicombe, 2006), and providing electrogenic shunts for phagocytic and endocytic processes (Beyenbach and Wieczorek, 2006). In the synaptic cleft, vesicle exocytosis is estimated to raise the pH 0.2–0.6 units, enabling the proton to act as a neurotransmitter by activating acid-sensing ion channels (ASICs) (Du et al., 2014). Gain of function mutations that create unregulated proton pores in voltage-gated cation channels have been implicated in myotonias, periodic paralysis, and some forms of Long QT Syndrome (Jurkat-Rott et al., 2012; Jurkat-Rott and Lehmann-Horn, 2010). Although these tiny “omega” currents are completely obscured by the central cation-conducting pore, the chronic leak of protons through these pores has been hypothesized to be sufficient to alter cardiac and muscular electrical activity (George, 2012; Jurkat-Rott et al., 2010; Moreau et al., 2015; Sokolov et al., 2007; Struyk et al., 2008). Given their varied physiological roles, proton transport proteins are viable therapeutic targets for treating human diseases—the most successful target has been the gastric proton pump, where irreversible inhibition of this proton flux mitigates gastrointestinal reflux disease (Sachs et al., 2007).

Electrical recordings have unequivocally established that ion accumulation and depletion occur at the plasma membrane during normal and pathophysiological activity. However, these whole cell electrical measurements do not directly reveal the identity of the transported ion(s), the subcellular location(s) of activity, or report on non-electrogenic transport events. In contrast, proton-sensitive mircoelectrodes provide a direct readout of the extracellular pH

(Fuster et al., 2004; Kreitzer et al., 2007), but only at a single macroscopic location abutting the cell. Because both techniques are time consuming, challenging, and provide negligible spatiotemporal information, various fluorescent imaging approaches have been employed to visualize changes in cellular pH. Genetically-encoded pH sensors and pH-sensitive fluorescent dextrans have been instrumental for measuring pH in the cytoplasm and intracellular compartments (Han and Burgess, 2010; Miesenbock et al., 1998); extracellular pH has been measured using fluorescein-conjugated wheat germ agglutinin (Stock et al., 2007). Although these reagents have enabled pH determinations at various locations in and around a cell, the real-time visualization of voltage-dependent proton fluxes at the plasma membrane has not been tenable with existing tools.

Here we use glycocalyx engineering (Laughlin and Bertozzi, 2007) to covalently label the cell surface with small molecule fluorescent pH sensors to visualize proton fluxes at the plasma membrane (Figure 1A). Using voltage-clamp fluorimetry to simultaneously control and visualize proton transport, we observed robust fluorescent signals that corresponded to cellular proton fluxes in both directions—outward and inward. The real-time kinetics of proton accumulation and depletion at the cell surface directly correlated to current density and buffer capacity, permitting the fluorescent signal to serve as a surrogate of ion channel and membrane transporter activity. The proton selectivity and sensitivity of the fluorescent signal enabled the determination of the proton current through chloride/proton antiporters (ClC-5) and the visualization of omega proton fluxes in the presence of a fully functioning voltage-gated Shaker potassium channel—where 6% of the total current was carried by protons. Strikingly, the resultant proton wavefront emanating from one cell was readily detected as it enveloped adjacent cells that were covalently modified with pH sensors.

Results

Chemistry, cell surface labeling and characterization

Compared to targeting or overexpressing a specific membrane protein, we hypothesized that a bioorthogonal chemical reaction with the cell's glycocalyx would result in a uniform and dense coating of fluorescent pH sensors at the cell surface to enable visualization of extracellular proton fluxes. To covalently modify the cell surface with small molecule fluorescent pH sensors, we used metabolic engineering with a membrane permeant peracetylated unnatural sugar to install azido groups into the cell's glycocalyx (Laughlin and Bertozzi, 2007; Saxon and Bertozzi, 2000), which were subsequently modified with pH-DIBO—an azido-reactive, rhodamine-based pH sensor (Figure 1A). The photoinduced electron transfer (PET) rhodamine pH sensor (pH-DIBO) was synthesized using a modified literature procedure (Aigner et al., 2012) where the piperazine groups were Boc-protected to simplify purification (Figure 1B). A pendant amino group was attached to **2** by first reaction with 2-ethylcarboxymercaptan followed by peptide coupling with 1,2-bis(2-aminoethoxy)ethane. Reaction of **4** with the 4-nitrobenyl ester of DIBO, and subsequent removal of the Boc groups with TFA yielded pH-DIBO in six steps from 3-(1-piperazinyl)phenol.

To fluorescently visualize proton fluxes using pH-DIBO, Chinese hamster ovary (CHO) cells were transiently transfected with a GFP-tagged, human voltage-gated proton channel

(Hv-1) and incubated with tetraacetylated N-azidoacetyl-D-mannosamine (azidosugar) (Laughlin and Bertozzi, 2007; Saxon and Bertozzi, 2000). After 2 d, the cells were labeled with pH-DIBO for 30 min and the currents and fluorescence were measured using patch-clamp fluorometry in a bath solution with a low buffer capacity (0.1 mM). Figure 2A shows families of currents and fluorescent signals from voltage-clamped CHO cells expressing Hv-1; HEK cells are shown in Figure S1. Voltage-activation of Hv-1 resulted in channel opening with voltage-dependent kinetics that reached steady state with test voltages greater than 20 mV. Simultaneous fluorescent imaging revealed that the fluorescent signals mirrored both the current magnitude and kinetics of voltage-activation at the various depolarizations. In contrast, Hv-1 channel closing at − 80 mV was much faster than the decaying fluorescent signal, consistent with the accumulated protons diffusing into bulk solution. Both the voltage-dependent currents and fluorescence signals were specific for Hv-1 channels because they were inhibited by Zn^{2+} (Figure S2) and required transfection with Hv-1 DNA (not shown). In addition, incubation with azidosugar was required to observe a significant change in fluorescence upon Hv-1 channel opening (Figure 2B). Cells incubated with azidosugar showed diffuse fluorescence over the entire cell with some higher intensity clusters (Figure 2B, inset). In contrast, the fluorescent signals from vehicle-treated cells were challenging to detect except for a few bright puncta. Because DIBO has been shown to react with thiols (van Geel et al., 2012), we chemically-inactivated pH-DIBO and repeated the labeling experiments. Comparing TIRF images of cells labeled with chemically-inactive or active pH-DIBO (Figure S3) revealed that the punctate labeling in the absence of azidosugar was due to pH-DIBO non-specifically modifying the cell surface. Although some background labeling occurs with the DIBO group, the cells must be incubated with azidosugar to coat the glycocalyx with enough pH sensors to fluorescently detect cellular proton fluxes.

Although the observed change in fluorescence was consistent with an outward proton flux, we wanted to confirm that the voltage-dependent changes in fluorescence were due to proton accumulation on the extracellular side of the membrane. To test this, we increased the buffer capacity in the external bath solution to compete with extracellularly-facing pH-DIBO sensors (Figure 2C). To normalize the cellular proton flux under each buffer condition, the cells were depolarized such that the same steady-state current (~ 250 pA) was reached after 4 s. As expected for extracellular proton accumulation, increasing the buffer capacity from 0.1 to 10 mM monotonically reduced the change in fluorescence until no change was detectable even though Hv-1 channels were open and conducting during the depolarizing test pulse (currents not shown). The competition between buffer and the glycocalyx-attached pH-DIBO sensors was also visualized by rapidly jumping to different depolarizing voltages and monitoring the rates to reach steady-state fluorescence (Figure S4). These supplementary experiments also ruled out saturation of the glycocalyx-attached sensors as the cause as the of the steady-state fluorescence. To convert the steady-state fluorescence into pH at the cell surface, we varied the pH of the bath solution and measured the change in fluorescence (Figure 2D). The fluorescence response of glycocalyx-attached pH-DIBO and pH-DIBO sensors in solution was linear over the same pH range, indicating that cell surface attachment did not appreciably change the pKa of the sensor. Thus, the 20% change in

fluorescence in Figure 2A corresponded to a pH of ~ 6.5 at the extracellular side of the membrane.

One component of the fluorescent signal that could not be easily explained was the biexponential decay kinetics that were observed when the channels were closed by repolarization (Figs. 2A, 2C, S1, S2, **and** S4). The slower time constant was consistent with proton diffusion because it was dependent on buffer concentration (Figure 2C); however, the initial drop in fluorescence was independent of buffer concentration. We initially dismissed inward proton currents through Hv-1 channels because the outward proton gradient used would require hyperpolarization less than − 90 mV. However, it has been recently shown that Hv-1 channels can deplete the local proton concentration on the intracellular side of the channel (De-la-Rosa et al., 2016), raising the possibility that the local proton driving force could be vastly different than the bulk proton gradient. Indeed, holding Hv-1 channels open for 4 s at 100 mV in the absence of a pH gradient created a substantial inward proton gradient, which was detected as an inward tail current when the channels were closed at 0 mV (Figure S5, blue trace). Under these experimental conditions (Figure S5), the fast component of the fluorescent decay was directly proportional to the channel closing rate, demonstrating that the initial drop in fluorescence was in fact due to protons re-entering the cell through Hv-1 channels before they closed.

We next examined whether the pH-DIBO signals correlated with Hv-1 channel localization by comparing the whole-cell fluorescent images. The pH-DIBO fluorescent image shows diffuse staining over the entire cell surface, though some large clusters of sensors were always observed as shown in the exemplar in Figure 2E. Surprisingly, Hv-1 channel localization was similar to pH-DIBO labeling, including the overlapping smiley emoji observed in both panels (Figure 2E**)**. Because Hv-1 channels cannot be N- or O-glycosylated (they do not contain any extracellular serines or threonines), we hypothesized that the funny convergence was due to pinocytosis of pH-DIBO-labeled glycoproteins into acidic compartments that overlapped with intracellular Hv-1 channels. Although the images collected contained both in- and out-of-focused light, we used the voltage-dependent change in the pH-DIBO signal to isolate the population of sensors that were facing the extracellular milieu. Figure 2F shows three $F - F_0$ snapshots before, during, and after a 100 mV test pulse (Movie S1). In contrast to the clusters observed in Figure 2E, the pH-DIBO signal in these processed images was scattered over the entire cell, indicating that functioning Hv-1 channels were not clustered, but were randomly distributed over the cell surface.

Disentangling proton efflux from ionic currents

To characterize the glycocalyx-attached pH sensors, we used a perfectly proton selective channel, Hv-1(Decoursey, 2003). However, many membrane transport proteins permit the simultaneous passage of a proton with a different ion or ions, which will contaminate or completely obscure the proton current. Omega currents from voltage-gated cation channels are a class of proton currents that have been postulated to cause several human diseases (George, 2012; Jurkat-Rott et al., 2010; Moreau et al., 2015; Sokolov et al., 2007; Struyk et al., 2008), but have not been observed without destroying or blocking the ion conducting pore domain. Therefore, we used our approach to determine whether these gain-of-function

voltage sensor domain mutations create omega proton currents in a channel with a functioning central pore. For the omega proton current, we used a Shaker-IR K^+ mutant (R371H) (Starace and Bezanilla, 2001), which is expected to form four voltage-dependent proton pores that circumscribe the central potassium pore (Figure 3A). Figure 3B shows current traces and fluorescent signals from cells expressing Shaker-IR R371H and WT channels. Depolarization-elicited Shaker-IR R371H currents activated rapidly and slowly inactivated over the 4-s depolarization. The rapid activation kinetics, large currents, and hallmark voltage-dependent C-type inactivation indicated that the majority of the current was flowing through the central pore. In contrast to the current traces, the changes in pH-DIBO fluorescence were indicative of a small, but relatively constant voltage-dependent proton current that modestly lowered the extracellular pH. Using the calibration in Figure 2D, the ~ 3% change in fluorescence at the end of the 120 mV pulse equated to a ~ 0.05 pH change on the extracellular side of the membrane. No omega proton fluxes were fluorescently detected with WT Shaker-IR, which expressed 10-fold more total current than the R371H mutant and had unusual inactivation kinetics with a 120 mV 4-s depolarization.

Because we could specifically visualize proton efflux in the presence of a functioning potassium pore, it was possible to calculate the omega proton current's contribution to the total current. To convert the pH-DIBO signal into current, we needed to determine whether the fluorescent signal could serve as a surrogate for the whole-cell proton current. Therefore, we compared the current traces and fluorescent signals from cells expressing the ClC-5 antiporter that transports two chloride ions for every exported proton (Figure 3A) (Zifarelli and Pusch, 2009). Cells expressing ClC-5 give rise to near instantaneous voltage-dependent currents that do not inactivate (Figure 3C). Both the magnitude and rate of $\Delta F/F_0$ proportionally increased with the total current, indicating that a constant proton source was activated with depolarization. These changes in fluorescence were proton-specific because they were not observed with a ClC-5 mutant (E211A) (Scheel et al., 2005) that only conducts chloride (Figure 3C, lower panels). To calibrate the fluorescent signals, we plotted the linear fits of $\Delta F/F_0$ vs current for Hv-1 and ClC-5 expressing cells (Figure 3D) and found that the slope of the ClC-5 data was approximately $1/3^{rd}$ of Hv-1. Because the fluorescent pH-DIBO signal was directly proportional to the whole-cell proton current, the maximum change in fluorescence for Shaker-IR R371H corresponded to ~ 40 pA of proton current (Figure 3B). Thus, the omega proton current is only 6% of the total Shaker-IR R371H current.

Visualizing extracellular proton depletion and proton wavefronts

In addition to the selective visualization and quantification of proton efflux in the presence of other ion currents, glycocalyx-attached pH-DIBO sensors should faithfully report on changes in proton concentration at the cell surface regardless of the proton source or direction. Therefore, we labeled cells expressing Shaker R362H (Starace and Bezanilla, 2004) with pH-DIBO to visualize inward proton currents at hyperpolarizing potentials (Figure 4A). To directly compare the inward fluorescent signals to the outward Hv-1 signals, we intentionally blocked the potassium channel pore (W434F) (Perozo et al., 1993); thus, the currents shown in Figure 4A are only omega currents. The change in fluorescence with Shaker-IR R362H was the mirror opposite to Hv-1 (Movie S3): the cell surface fluorescence

became dimmer upon hyperpolarization, reached steady-state, and then rapidly recovered with biexponential kinetics when the cell was returned to the 30 mV holding potential (Figure 4A, bottom panel). In addition, the absolute value of the current-$\Delta F/F_0$ slope (0.82 ± 0.09) was similar to Hv-1, indicating that Shaker-IR R362H is a proton selective omega current that readily depletes protons on the extracellular side of the membrane.

While performing the proton flux experiments, we noticed the pH-DIBO-labeled cells adjacent to the patch-clamped cell fluoresced with a delayed synchrony, as if the neighboring cells were reporting on the proton efflux of the depolarized cell (Movie S5). To test this supposition, we measured the change in fluorescence on each half of a neighboring cell (near and far) and plotted it against the voltage-clamped cell expressing Hv-1 channels (Figure 4B). The clamped, near, and far fluorescent signals were consistent with a proton wavefront originating from the clamped cell that first reached the near side of the adjacent cell and then gradually enveloped the far side of the cell. After a 4s depolarization, the extracellular proton concentration was the greatest around the clamped cell, but a substantial proton gradient was also detected over the surface of the neighboring cell that was four microns away. Upon turning off the proton source (clamped cell), the extracellular proton gradient across the neighboring cell decayed with a single time constant (Figure 4B, right panel), reaffirming that the rapid drop in fluorescence observed with the patch-clamped cells was due to protons rapidly entering the cytoplasm before Hv-1 channel closure. As expected for an extracellular proton wavefront, the pH surrounding a neighboring cell was titratable with buffer concentration (Figure 4C). In total, these data demonstrated that the glycocalyx-attached pH-DIBO sensors exquisitely report on the extracellular pH at the plasma membrane, enabling the visualization of both proton fluxes and wavefronts.

Discussion

By covalently attaching small molecule pH-sensitive fluorophores (pH-DIBO) directly to the cell's glycocalyx, we observed both inward and outward proton fluxes, extracellular pH gradients, and proton wavefronts enveloping neighboring cells. Although a subpopulation of sensors is internalized, these luminally-facing fluorescent sensors are unresponsive to plasma membrane activity. As designed, the glycocalyx-attached pH-DIBO sensors did not report on ion channel gating or transporter activation/deactivation, but rather the kinetics of proton accumulation or depletion on the extracellular side of the membrane. The juxtaposition of the covalently-attached pH-DIBO sensors to the extracellular vestibules of membrane transport proteins provided remarkable insight into the extracellular pH environment abutting a mammalian cell. Previous determinations of extracellular pH at the cell surface required either extremely large cells (Zifarelli and Pusch, 2009) or mathematical modeling (Zifarelli et al., 2008) to estimate the radiating pH gradient. Our results suggest that Hv-1 proton channels create a much more acidic extracellular environment than was previously calculated. For example, the pH surrounding the clamped cell in Figure 4B is ~ 6.3 whereas the calculation (Zifarelli et al., 2008) for a similarly-sized spherical cell is ~7.2. Part of the difference may be due to limited proton diffusion in the restricted space between the cell and the glass coverslip. However, the pH gradient (6.8 – 7.2) observed across neighboring cells indicates that the majority of the protons emanating from a patch clamped cell are freely diffusing in the bath solution. These proton accumulation and diffusion results

also highlight that open Hv-1 channels not only deplete the local intracellular proton concentration (De-la-Rosa et al., 2016), but also raise the extracellular proton concentration tens of microns away from the cell perimeter.

Because the glycocalyx-attached pH sensors are well within the experimentally and computationally determined unstirred layer (USL) for protons (Pohl et al., 1998), our approach provides an opportunity to monitor proton diffusion over the entire cell surface during proton transport. The slow opening and closing of Hv-1 channels confounds modeling these data; however, the fluorescent data from the rapidly closing Shaker R362H omega pores (Figure 4A) are amenable to fitting. Proton depletion from the glycocalyx shell upon channel opening could be well fitted with a simple equation:

$$[cell] \xleftarrow{k_{in}} [shell] \xleftrightarrow{K_B} [bulk]$$

where *shell* corresponded to the approximate volume of the cell's glycocalyx, K_B was the proton equilibrium constant between *bulk* and *shell*, and k_{in} correlated with the steady state current at each depolarizing voltage. However upon channel closing, the model failed to recapitulate the slow phase of the biphasic kinetics of proton replenishing shown in Figure 4A (bottom panel); therefore, an additional layer (*USL*) and equilibrium constant (K_{USL}) between the glycocalyx shell and an unstirred layer was added to the model (Figure 4D). For the modeling, we varied k_{in}, the volumes of the *USL* and *shell*, and the rate of proton entry and exit into a layer. In addition, we assumed the equilibrium constant between any layer was equal to one and the forward and backward proton rates into a layer (*shell*, *USL*, and *bulk*) was the same. At each voltage (Figure 4E), k_{in} was varied to achieve the steady state fluorescence after 4 s, which correlated well with the total number of protons that entered the cell (average current) during the hyperpolarizing pulse (Figure 4A, top panel). In contrast to the simple shell model, this concentric volume model fit the biphasic return of protons to the glycocalyx shell (Figure 4E). Because k_{in} was held constant at each voltage, the model poorly fit the kinetics of proton influx at hyperpolarizing voltages where channel gating, and thus current, was not constant during the test pulse (Figure 4A, top panel). In addition, the local proton concentration in the *shell* and equilibrium between the layers is likely more complicated due to the cell surface proteins, carbohydrates, and covalently-bound pH sensors in the glycocalyx.

Although we could fit the fluorescent signal kinetics of proton replenishing at the cell surface, the model does not speak to how the unstirred layer fills (or empties) during proton transport. Several studies (Branden et al., 2006; Mulkidjanian et al., 2006; Serowy et al., 2003; Springer et al., 2011) suggest that during proton efflux the protons diffuse rapidly and parallel to the plasma membrane before entering the unstirred layer and bulk solution. The neighboring cell experiments in Figure 4B and 4C demonstrate that it is experimentally feasible to utilize glycocalyx-attached pH sensors to spatiotemporally detect pH differences at the plasma membrane. However, in our experiments, the proton channels and transport proteins were randomly distributed over the entire cell surface; thus, we did not detect rapid proton diffusion parallel to the plasma membrane upon activating proton efflux with voltage. Visualization of proton efflux from a proton transport protein that localizes to a specific

region of the plasma membrane would provide insight on whether protons rapidly circumscribe a living cell before diffusing into the unstirred layer and bulk solution.

An unexpected advantage of directly attaching the sensors to the glycocalyx was that the change in pH-DIBO fluorescence was an accurate approximation of the whole cell proton current in voltage-clamp experiments. By comparing the ClC-5 current-$\Delta F/F_0$ slope to Hv-1, we showed that only 1/3rd of the ClC-5 current is carried by protons, fully consistent with the known 2:1 stoichiometry of its transport cycle (Zifarelli and Pusch, 2009). In contrast to ClC-5, Shaker-IR omega currents were as proton-selective as Hv-1 channels. Using the current-$\Delta F/F_0$ relationship, we estimated that the proton current accounted for ~ 6% of the total current for a Shaker-IR VSD omega mutant. If all four VSDs pass the same amount of proton current, then our experimental results indicate that a single omega pore contributes 1 - 2% of the total current in a voltage-gated K^+ channel. Because VSD mutations affect the potassium current through the central pore by shifting the voltage-activation, deactivation, and inactivation of the channel, we expect the proton current's contribution to the total current will vary for the different omega pore mutants that cause human disease. No proton fluxes were ever observed with wild-type voltage-gated K^+ channels, confirming that the histidine residues in the VSDs are required for the omega current in full-length Shaker-IR channels. In addition to being a surrogate for proton current, voltage-clamp fluorometry with pH-DIBO will also be useful for identifying residues required for proton permeation and exploring the voltage-dependency of non-electrogenic proton transport proteins.

Because proton transport is involved in a wide range of cellular processes, chemical tools that specifically detect plasma membrane proton fluxes have broad utility. The diverse color and pKa palette of small molecule proton sensors (Han and Burgess, 2010) provides additional flexibility to coat cells with fluorophores with desirable pH-sensing and photophysical properties. Combining our chemical approach with state-of-the-art imaging techniques will allow for high-resolution spatiotemporal imaging over the entire landscape of a cell and possibly visualization of single-channel fluxes. Given that the glycocalyces of living organisms can be engineered with unnatural sugars (Laughlin et al., 2008; Laughlin and Bertozzi, 2009; Xie et al., 2016), visualization of rapid efflux from cells, tissues, and model organisms is tenable by modifying metabolically-labeled glycocalyces with small molecule ion- or metabolite-sensitive fluorophores.

Significance

Proton fluxes at the plasma membrane are vital for maintaining intracellular and extracellular pH as well as a serving as a counter-ion for the cellular transport of amino acids, lactate, and other mono- and dicarboxylates. Current biophysical and biological approaches have been unable to visualize voltage-dependent proton fluxes over the entire plasma membrane of a mammalian cell. We developed a cell surface chemistry approach to visualize proton fluxes at the plasma membrane by covalently attaching small molecule, pH-sensitive fluorophores to the glycocalyx of mammalian cells metabolically-labeled with an unnatural azidosugar. The dense coating of extracellularly-facing sensors provided real-time detection of proton accumulation and depletion at the plasma membrane from voltage-gated proton channels, antiporters, and proton leak channels associated with human disease.

Moreover, the proton wavefront emanating from one cell was clearly visible when it enveloped nearby neighboring cells. The modularity of our approach makes it adaptable to study any plasma membrane transport protein that increases the extracellular substrate concentration in native cells, tissues and model organisms.

Experimental Procedures

Synthetic Protocols

Protocols and characterization of all new compounds are described in the supplementary information. An α/β anomer mixture of tetraacetylated N-Azidoacetyl-D-mannosamine (azido-sugar); 5,6-dihydro-11,12-didehydro-dibenzo[a,e]cycloocten-5-yl ester, 4-nitrophenyl ester (DIBO-4-nitrophenyl ester), and Compound 1 were synthesized following procedures described in the literature.

Plasmids and cDNAs

Plasmids containing human GFP-Hv-1, ClC5, and Shaker-IR omega mutants were gifts from David Clapham (Harvard Medical School), Michael Pusch (Istituto di Biofisica), and Baron Chanda (University of Wisconsin–Madison), respectively. Mutations were introduced by QuikChange site-directed mutagenesis (Agilent) and confirmed by DNA sequencing the entire gene.

Cell culture, transfections and pH-DIBO cell surface labeling

Chinese Hamster Ovary-K1 (CHO) cells were cultured in F-12K nutrient mixture (Invitrogen); HEK cells were cultured in high glucose DMEM medium. All media were supplemented with 10% fetal bovine serum (Hyclone) and 100 units/mL penicillin/streptomycin (Invitrogen). The cells were plated at 60 75% confluency in 35 mm dishes. Glass bottom culture dishes (MatTek) were used for HEK cells. After 24 h, Cells were transiently transfected with a 1 μg of ion channel or transporter DNA and 8 μL of Lipofectamine (Invitrogen) for CHO cells or 4 μL of Lipofectamine and 6uL PLUSTM reagent (Invitrogen) for HEK cells in Opti-MEM (Invitrogen). To visualize transfected cells, 0.25 μg of pEGFP-C3 was added to transfections that did not contain GFP-tagged channels/transporters. After terminating the transfections, the cells were incubated in media containing 50 μM azido-sugar for 2 d, which was replenished after 24 h.

Whole Cell Patch Clamp Fluorometry

Transfected CHO cells were trypsinized and seeded on a glass bottom culture dish for 2 h and then labeled with pH-DIBO (50 μM) in Opti-MEM at r.t. for 0.5 h; HEK cells were directly labeled with pH-DIBO in Opti-MEM. Transfected cells were identified using an inverted light microscope (Axiovert 40 CFL; Carl Zeiss, Inc.) and the currents were recorded in the whole cell patch configuration at room temperature (24 ± 2°C) using a glass electrode (pipette resistance: 2.5 – 3.5 MΩ) filled with (in mM): 126 NaCl, 2 $MgSO_4$, 0.5 $CaCl_2$, 5 EGTA 4 K_2-ATP, 0.4 GTP and 25 buffer (HEPES for pH = 7.5 and 7.0, MES for pH = 6.0) with NaOH; bath solution contained (in mM): 145 NaCl, 5.4 KCl, 5 $CaCl_2$, 0.1 buffer (TAPS for pH = 8.0, HEPES for pH = 7.5 and 7.0, Bis-Tris for pH = 6.5, MES for pH = 6.0) with NaOH. Cells were imaged at 10 Hz using a CoolLED pE-4000 light source (exposure

time = 10 ms), 63 × 1.4 N.A. oil immersion objective, and a Zyla sCMOS camera (ANDOR). GFP and pH-DIBO were excited respectively at 460 nm channel (light power = 30%, emission filter set 38 HE from Zeiss) and 550 nm channel (light power = 15%, emission filter set 20 HE from Zeiss). The patch clamp (Axopatch 200B), light source, and camera were controlled with Clampex 10.5 (Molecular Devices); fluorescent images were collected (10 Hz, 4 × 4 binning) and processed using open source software (micro-manager and ImageJ). F_0 is the average fluorescence intensity of the first five data points before the test depolarization.

Supplementary Material

Refer to Web version on PubMed Central for supplementary material.

Acknowledgements

This work was supported by a grant to WRK from the National Institutes of Health (GM-070650). WRK thanks Dr. Anthony Carruthers for his wizardry with the BerkeleyMadonna kinetic modeling software.

References

Aigner D, Borisov SM, Fernandez FJ, Fernandez Sanchez JF, Saf R, Klimant I. New fluorescent pH sensors based on covalently linkable PET rhodamines. Talanta. 2012; 99:194–201. [PubMed: 22967541]

Beyenbach KW, Wieczorek H. The V-type H+ ATPase: molecular structure and function, physiological roles and regulation. J Exp Biol. 2006; 209:577–589. [PubMed: 16449553]

Branden M, Sanden T, Brzezinski P, Widengren J. Localized proton microcircuits at the biological membrane-water interface. Proc Natl Acad Sci U S A. 2006; 103:19766–19770. [PubMed: 17172452]

De-la-Rosa V, Suarez-Delgado E, Rangel-Yescas GE, Islas LD. Currents through Hv1 channels deplete protons in their vicinity. J Gen Physiol. 2016; 147:127–136. [PubMed: 26809792]

Decoursey TE. Voltage-gated proton channels and other proton transfer pathways. Physiol Rev. 2003; 83:475–579. [PubMed: 12663866]

Du J, Reznikov LR, Price MP, Zha XM, Lu Y, Moninger TO, Wemmie JA, Welsh MJ. Protons are a neurotransmitter that regulates synaptic plasticity in the lateral amygdala. Proc Natl Acad Sci U S A. 2014; 111:8961–8966. [PubMed: 24889629]

Fischer H, Widdicombe JH. Mechanisms of acid and base secretion by the airway epithelium. J Membr Biol. 2006; 211:139–150. [PubMed: 17091214]

Fuster D, Moe OW, Hilgemann DW. Lipid- and mechanosensitivities of sodium/hydrogen exchangers analyzed by electrical methods. Proc Natl Acad Sci U S A. 2004; 101:10482–10487. [PubMed: 15240890]

George AL Jr. Leaky channels make weak muscles. J Clin Invest. 2012; 122:4333–4336. [PubMed: 23187135]

Han J, Burgess K. Fluorescent indicators for intracellular pH. Chem Rev. 2010; 110:2709–2728. [PubMed: 19831417]

Jurkat-Rott K, Groome J, Lehmann-Horn F. Pathophysiological role of omega pore current in channelopathies. Front Pharmacol. 2012; 3:112. [PubMed: 22701429]

Jurkat-Rott K, Holzherr B, Fauler M, Lehmann-Horn F. Sodium channelopathies of skeletal muscle result from gain or loss of function. Pflugers Arch. 2010; 460:239–248. [PubMed: 20237798]

Jurkat-Rott K, Lehmann-Horn F. State of the art in hereditary muscle channelopathies. Acta Myol. 2010; 29:343–350. [PubMed: 21314017]

Kopic S, Geibel JP. Gastric acid, calcium absorption, and their impact on bone health. Physiol Rev. 2013; 93:189–268. [PubMed: 23303909]

Kreitzer MA, Collis LP, Molina AJ, Smith PJ, Malchow RP. Modulation of extracellular proton fluxes from retinal horizontal cells of the catfish by depolarization and glutamate. J Gen Physiol. 2007; 130:169–182. [PubMed: 17664345]

Laughlin ST, Baskin JM, Amacher SL, Bertozzi CR. In vivo imaging of membrane-associated glycans in developing zebrafish. Science. 2008; 320:664–667. [PubMed: 18451302]

Laughlin ST, Bertozzi CR. Metabolic labeling of glycans with azido sugars and subsequent glycan-profiling and visualization via Staudinger ligation. Nat Protoc. 2007; 2:2930–2944. [PubMed: 18007630]

Laughlin ST, Bertozzi CR. In vivo imaging of Caenorhabditis elegans glycans. ACS Chem Biol. 2009; 4:1068–1072. [PubMed: 19954190]

Miesenbock G, De Angelis DA, Rothman JE. Visualizing secretion and synaptic transmission with pH-sensitive green fluorescent proteins. Nature. 1998; 394:192–195. [PubMed: 9671304]

Moreau A, Gosselin-Badaroudine P, Chahine M. Gating pore currents, a new pathological mechanism underlying cardiac arrhythmias associated with dilated cardiomyopathy. Channels (Austin). 2015; 9:139–144. [PubMed: 26046592]

Mulkidjanian AY, Heberle J, Cherepanov DA. Protons @ interfaces: implications for biological energy conversion. Biochim Biophys Acta. 2006; 1757:913–930. [PubMed: 16624250]

Perozo E, MacKinnon R, Bezanilla F, Stefani E. Gating currents from a nonconducting mutant reveal open-closed conformations in Shaker K+ channels. Neuron. 1993; 11:353–358. [PubMed: 8352943]

Pohl P, Saparov SM, Antonenko YN. The size of the unstirred layer as a function of the solute diffusion coefficient. Biophys J. 1998; 75:1403–1409. [PubMed: 9726941]

Sachs G, Shin JM, Vagin O, Lambrecht N, Yakubov I, Munson K. The gastric H,K ATPase as a drug target: past, present, and future. J Clin Gastroenterol. 2007; 41(Suppl 2):S226–242. [PubMed: 17575528]

Saxon E, Bertozzi CR. Cell surface engineering by a modified Staudinger reaction. Science. 2000; 287:2007–2010. [PubMed: 10720325]

Scheel O, Zdebik AA, Lourdel S, Jentsch TJ. Voltage-dependent electrogenic chloride/proton exchange by endosomal CLC proteins. Nature. 2005; 436:424–427. [PubMed: 16034422]

Serowy S, Saparov SM, Antonenko YN, Kozlovsky W, Hagen V, Pohl P. Structural proton diffusion along lipid bilayers. Biophys J. 2003; 84:1031–1037. [PubMed: 12547784]

Sokolov S, Scheuer T, Catterall WA. Gating pore current in an inherited ion channelopathy. Nature. 2007; 446:76–78. [PubMed: 17330043]

Springer A, Hagen V, Cherepanov DA, Antonenko YN, Pohl P. Protons migrate along interfacial water without significant contributions from jumps between ionizable groups on the membrane surface. Proc Natl Acad Sci U S A. 2011; 108:14461–14466. [PubMed: 21859952]

Starace DM, Bezanilla F. Histidine scanning mutagenesis of basic residues of the S4 segment of the shaker k+ channel. J Gen Physiol. 2001; 117:469–490. [PubMed: 11331357]

Starace DM, Bezanilla F. A proton pore in a potassium channel voltage sensor reveals a focused electric field. Nature. 2004; 427:548–553. [PubMed: 14765197]

Stock C, Mueller M, Kraehling H, Mally S, Noel J, Eder C, Schwab A. pH nanoenvironment at the surface of single melanoma cells. Cell Physiol Biochem. 2007; 20:679–686. [PubMed: 17762194]

Struyk AF, Markin VS, Francis D, Cannon SC. Gating pore currents in DIIS4 mutations of NaV1.4 associated with periodic paralysis: saturation of ion flux and implications for disease pathogenesis. J Gen Physiol. 2008; 132:447–464. [PubMed: 18824591]

van Geel R, Pruijn GJ, van Delft FL, Boelens WC. Preventing thiol-yne addition improves the specificity of strain-promoted azide-alkyne cycloaddition. Bioconjug Chem. 2012; 23:392–398. [PubMed: 22372991]

Xie R, Dong L, Du Y, Zhu Y, Hua R, Zhang C, Chen X. In vivo metabolic labeling of sialoglycans in the mouse brain by using a liposome-assisted bioorthogonal reporter strategy. Proc Natl Acad Sci U S A. 2016; 113:5173–5178. [PubMed: 27125855]

Zifarelli G, Pusch M. Conversion of the 2 Cl(−)/1 H+ antiporter ClC-5 in a NO3(−)/H+ antiporter by a single point mutation. Embo J. 2009; 28:175–182. [PubMed: 19131966]

Zifarelli G, Soliani P, Pusch M. Buffered diffusion around a spherical proton pumping cell: a theoretical analysis. Biophys J. 2008; 94:53–62. [PubMed: 17827236]

Highlights

- Glycocalyx-attached pH sensors enable spatiotemporal detection of proton fluxes.
- Fluorescent pH signals provide a direct readout of cell surface proton activity.
- Proton leak channels associated with human diseases were visualized.
- Proton wavefronts were detected as they enveloped neighboring cells.

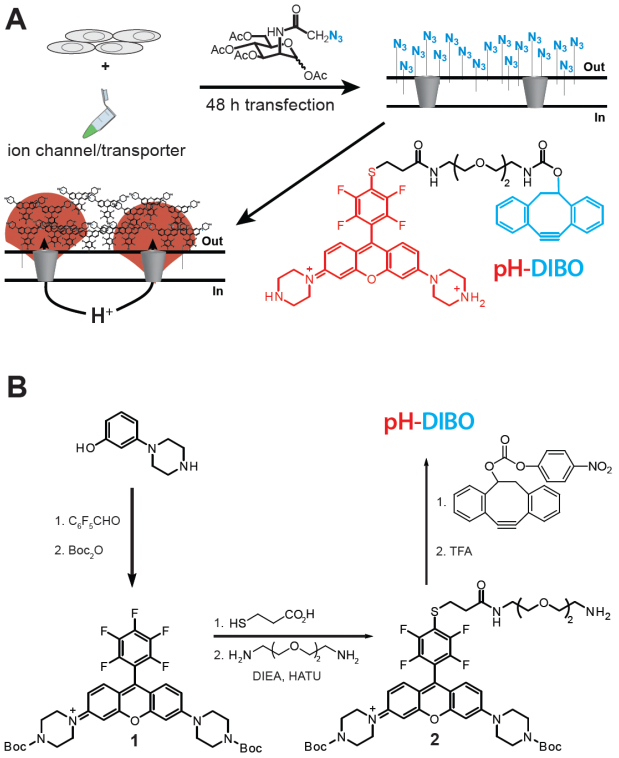

Figure 1.

Glycocalyx engineering strategy to visualize plasma membrane proton fluxes: (**A**) Cells expressing ion channels or membrane transporters are incubated with an azidosugar (azido group in blue) and the cell surface is subsequently labeled with a fluorescent pH sensor (pH-DIBO) to detect proton fluxes. The azide-reactive and fluorescent pH-sensitive groups in the chemical structure and label are colored blue and red, respectively. (**B**) Scheme for the synthesis of pH-DIBO.

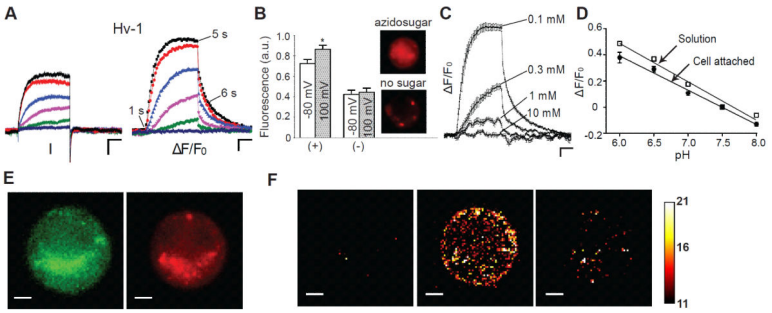

Figure 2.

Visualization of proton efflux from CHO cells expressing Hv-1: (**A**) Voltage-clamp fluorometry (VCF) traces: the cell was held at − 80 mV, and currents and fluorescence were elicited from 4-s command voltages from 0 to 100 mV in 20-mV increments. (**B**) Average normalized fluorescence at − 80 mV and after a 4-s depolarization (100 mV) in the presence (+) or absence (−) of azidosugar. Data were averaged from 5 cells ± SEM; asterisk indicates significance of at least $P < 0.05$. *Inset:* Images of cells labeled with (top) or without (bottom) azidosugar. (**C**) Fluorescence traces of cells expressing similar total current (150 – 300 pA) in bath solutions with various buffer concentrations (HEPES); n = 5; error bars are ± SEM. (**D**) Change in pH-DIBO fluorescence attached to the cell surface (filled circles) and in a solution (open squares) versus pH. Buffer concentration 10 mM; $\Delta F/F_0$ at pH 7.5 was defined as 0; data were averaged 5 – 10 experiments ± SEM. (**E**) GFP and pH-DIBO fluorescence images (10 ms) of CHO cells expressing Hv-1. (**F**) $\Delta F/F_0$ snapshots of pH-DIBO fluorescence at 100 mV at time points indicated in (A). VCF scale bars represent 50 pA, 2% $\Delta F/F_0$, and 1 s; fluorescent image scale bars are 5 μm; pH_o/pH_i = 7.5/6.0; bath solution 0.1 mM HEPES except in (**C** and **D**).

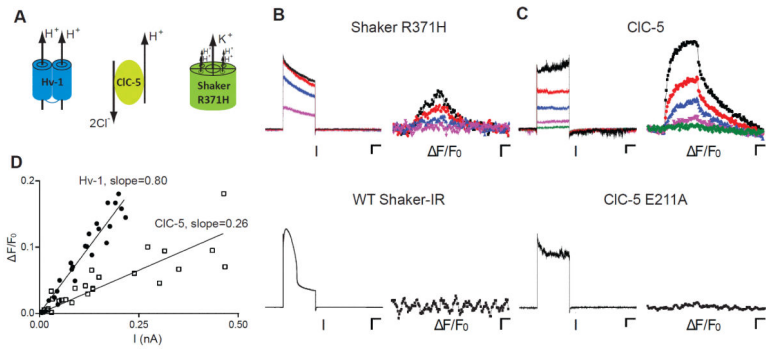

Figure 3.

Visualization of proton efflux from co-transport proteins expressed in CHO cells: (**A**) Cartoons of Hv-1, ClC-5 antiporter, and Shaker omega pore mutant (R371H). (**B**) Voltage-clamp fluorometry (VCF) current and fluorescence traces of cells expressing Shaker R371H (scale bars 100 pA, 1%, 1 s) from 0 to 120 mV in 40-mV increments and WT Shaker-IR at 120 mV (scale bars 1 nA, 1%, 1 s); holding potential − 80 mV; pH_o/pH_i = 7.5/6.0 (bath: 0.1 mM HEPES). (**C**) VCF current and fluorescence traces of cells expressing ClC-5 from 60 to 140 mV in 20-mV increments or ClC-5 E211A at 140 mV. Scale bars 50 pA, 2%, 1 s; holding potential − 80 mV; pH_o/pH_i = 7.5/7.5 (bath: 0.1 mM HEPES). (**D**) Plot of $\Delta F/F_0$ as a function of current for Hv-1 (filled circles) and ClC-5 (open squares).

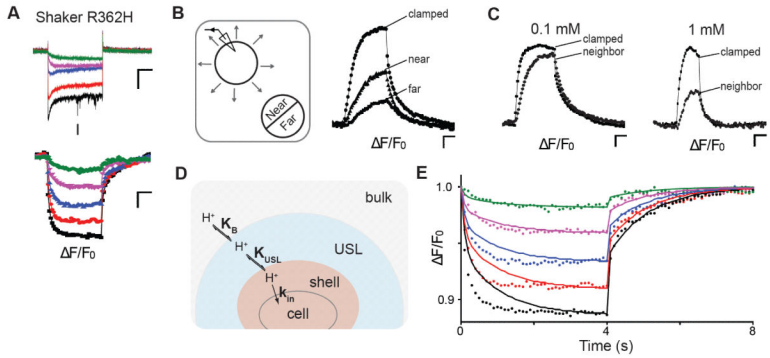

Figure 4.

Visualization of extracellular proton depletion and wavefronts in CHO cells: (**A**) Voltage-clamp fluorometry traces of cells expressing Shaker R362H: the cell was held at 30 mV, and currents and fluorescence were elicited from 4-s command voltages from − 40 to − 120 mV in 20-mV increments; scale bars 50 pA, 2%, 1 s, pH_o/pH_i = 6.0/7.5 (bath: 0.1 mM MES); (**B**) *Left*: Cartoon of proton diffusion to a neighboring cell. *Right*: Fluorescence signals of pH-DIBO-labeled cells. A voltage-clamped Hv-1 expressing cell (− 80 mV) was depolarized to 100 mV and the fluorescent signals from the clamped (d = 23 μm) and a neighboring cell (near and far side, d = 18 μm) were plotted versus time. The distance of the two cells is ~ 4 μm; scale bars 2%, 1 s, pH_o/pH_i = 7.5/6.0 (bath: 0.1 mM HEPES). (**C**) Buffer concentration dependence of the fluorescent signals of a neighboring cell ~ 8 μm away from an Hv-1 expressing cell. The clamped cells were held at − 80 mV, depolarized to 100 mV, and the fluorescence of the clamped and neighboring cells were plotted versus time. Scale bars 2%, 1 s, pH_o/pH_i = 7.5/6.0; (bath: 0.1 mM HEPES). (**D**) Cartoon diagram and proton diffusion equation of the concentric volume model with an unstirred layer (*USL*). (**E**) Fits of the fluorescent data in (A). *Bulk* = 1 mL; *USL* = 1.5 fL; *shell* = 0.08 fL; $K_{USL} = K_B = 1$; $k_f = k_r = 1.4\ s^{-1}$; k_{in} (black) = 0.090 s^{-1}; k_{in} (red) = 0.070 s^{-1}; k_{in} (blue) = 0.050 s^{-1}; k_{in} (magenta) = 0.030 s^{-1}; k_{in} (green) = 0.013 s^{-1}..